https://doi.org/10.5194/essd-2026-476
Preprint. Discussion started: 31 August 2026

Open Access Earth System Science Data Discussions

A Spray-Mediated Surface Turbulent Heat Flux Dataset for the Southern Ocean

An Yi[1], Jiping Liu[*1], Ian A. Renfrew[2], Chaoyun Yang[1], Changming Dong[3], Xiangzhou Song[4], Qinghua Yang[1]

[1]School of Atmospheric Sciences, Sun Yat-sen University and Southern Marine Science and Engineering Guangdong Laboratory (Zhuhai), Zhuhai, 519082, China
[2]School of Environmental Sciences, University of East Anglia, Norwich, NR4 7TJ, UK
[3]School of Marine Sciences, Nanjing University of Information Science and Technology, Nanjing, 210044, China
[4]Key Laboratory of Marine Hazards Forecasting, Ministry of Natural Resources (MNR), Hohai University, Nanjing, 210024, China

Correspondence to: Jiping Liu (liujp63@mail.sysu.edu.cn)

Abstract. Sea spray generated by wave breaking under high wind speeds strongly influences air-sea turbulent heat exchange. Nowhere is this process more critical than the Southern Ocean where the most extreme wave climate on Earth is located. However, current existing gridded air-sea heat flux datasets lack representation of sea spray-mediated component, which lead to a major problem in assessing and understanding the role of sea spray in the Southern Ocean. Here, we present a new gridded dataset of spray-mediated latent and sensible heat fluxes over the Southern Ocean that incorporates a full sea spray microphysical model, which considers spray generation that depends on regional wind and wave states. Our data allows a quantitative assessment of the spray-mediated contribution to the total air-sea heat flux exchange. Climatologically, spray-mediated heat fluxes range from 0.04 to 39.6 W m^{-2}, with large fluxes in the circumpolar region (50°S-60°S), especially in the Indian sector during austral winter. Validation of an extreme cyclone shows that, within the high wind sector of the cyclone, spray-mediated heat fluxes double the regional fluxes compared to conventional bulk algorithm estimates. This dataset serves a critical foundation for examining the Southern Ocean's role in the global energy budget.

1 Introduction

Turbulent heat fluxes, comprising latent (LHF) and sensible heat fluxes (SHF), are a fundamental physical quantity characterizing heat and moisture exchange between the ocean and atmosphere—a process primarily driven by molecular and turbulent diffusion processes within the surface layer (Andreas, 1992; Fairall et al., 1990). Given the scarcity of direct measurements, currently, surface turbulent fluxes are typically estimated from bulk aerodynamic formulae as a function of input surface meteorological variables, including wind speed, air-sea humidity and temperature gradients (Liu et al., 1979). The surface meteorological variables required as input into the bulk flux model can be obtained from three primary sources: in-situ measurements (research vessels, buoys, voluntary observing ships or aircraft; e.g., Josey et al., 2014), numerical weather prediction model output, such as reanalysis or operational analysis products (e.g., ERA5; Hersbach, 2023), and

https://doi.org/10.5194/essd-2026-476
Preprint. Discussion started: 31 August 2026

satellite data products (e.g., J-OFURO3; Tomita et al., 2019). However, the Southern Ocean is grossly under-surveyed by traditional observations due to the remoteness of the area and harsh environment, causing the largest data gap in the world's oceans (Bourassa et al., 2013; Swart et al., 2019).

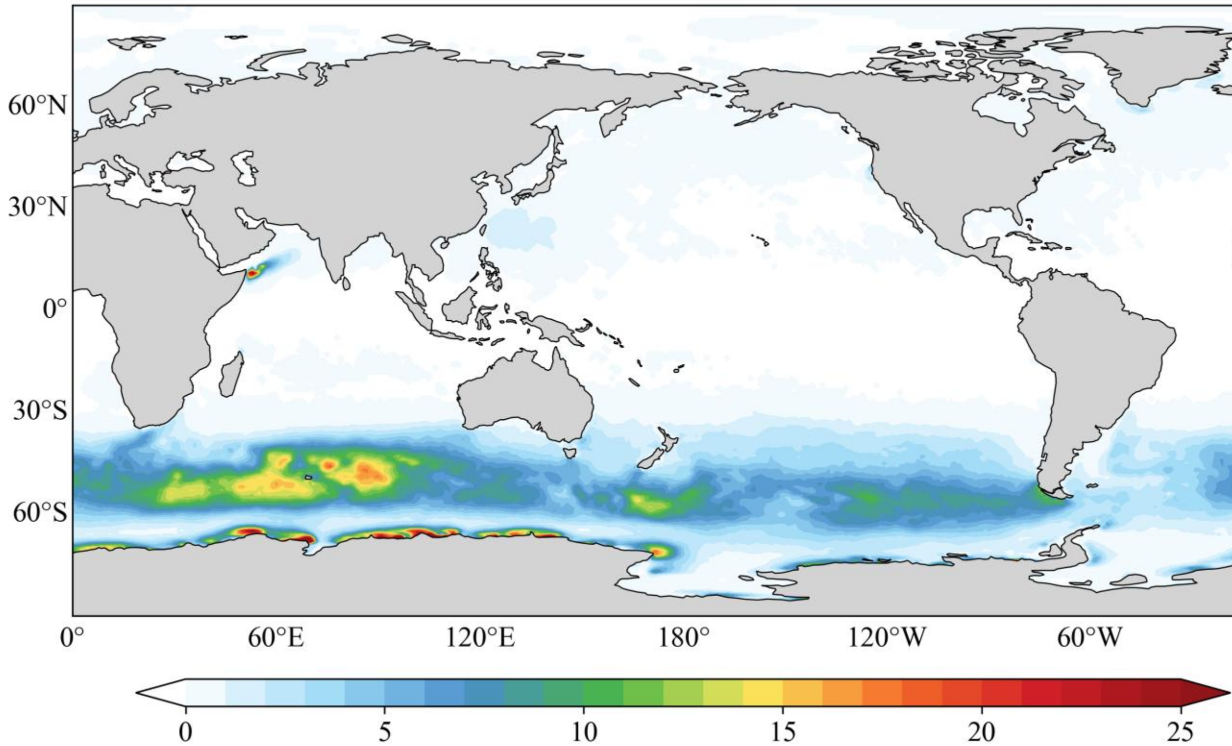

Figure 1: Summer climatology (June-July-August) of the frequency of high-winds (> 15 m s^{-1}) (unit: %) calculated from the daily ERA5 sea surface winds for the period 1993-2022.

The Southern Ocean is renowned for the "Roaring Forties" westerlies, hosting the climatologically strongest surface winds and extreme waves of any open ocean area (Young et al., 2011; Young and Ribal, 2019; Yuan, 2004), thereby fostering strong heat, moisture, and momentum exchanges between the ocean and atmosphere (Babanin, 2011; Bourassa et al., 2013; Liu et al., 2011). Here, high winds (> 15 m s^{-1}) are 5–7 times more frequent, and wave heights (4–6 m) are 2–3 times larger than in other ocean basins (Figs. 1 and 2; Note that although large wind and wave activities also occur in the Northern Hemisphere during DJF, they are largely confined to the North Pacific and North Atlantic storm tracks). Consequently, breaking waves and whitecaps (Anguelova and Webster, 2006; Deike, 2022) inject massive sea spray via bursting bubbles and torn crests, effectively increasing the oceanic surface area (Bortkovskii, 2013; Makin, 1998; Troitskaya et al., 2017). Thus, turbulent heat transfer is no longer confined to the sea surface but instead extends vertically into the spray-filled boundary layer (Richter and Sullivan, 2014). Relying solely on surface variables, traditional bulk formulae are inherently inadequate for capturing this enhanced heat exchange under high-wind conditions (Andreas et al., 2015; Veron, 2015).

https://doi.org/10.5194/essd-2026-476
Preprint. Discussion started: 31 August 2026

Open Access Earth System Science Data Discussions

Hence, explicitly accounting for these spray-mediated processes is essential for accurate representation of the surface heat budget in the Southern Ocean.

The profound impact of sea spray processes is extensively documented in tropical cyclone studies. Using a Tropical Cyclone Model (TCM3) with explicit cloud microphysics, Wang et al. (2001) showed spray increases total enthalpy flux by approximately 20%. In idealized simulations using the nonhydrostatic MM5, Gall et al. (2008) found spray boosted SHF and LHF by roughly 200 W m^{-2} and more than 150 W m^{-2}, respectively, intensifying storms by over 10 mb. Similarly, integrating spray into an NWP model based on Monin-Obukhov Similarity Theory, Bao et al. (2011) doubled maximum SHF and increased LHF by 10%. Recognizing wave-state modulation, Barr et al. (2023) utilized a fully coupled atmosphere-wave-ocean model, revealing a 5–20% enthalpy flux enhancement under 40–50 m s^{-1} winds. Collectively, these results demonstrate that enhanced spray-mediated heat transfer is a vital component of the high-wind surface energy budget, serving as critical thermodynamic fuel for storms. Consequently, neglecting these effects limits the ability of coupled models to reproduce observed rapid storm intensification (Xu et al., 2022).

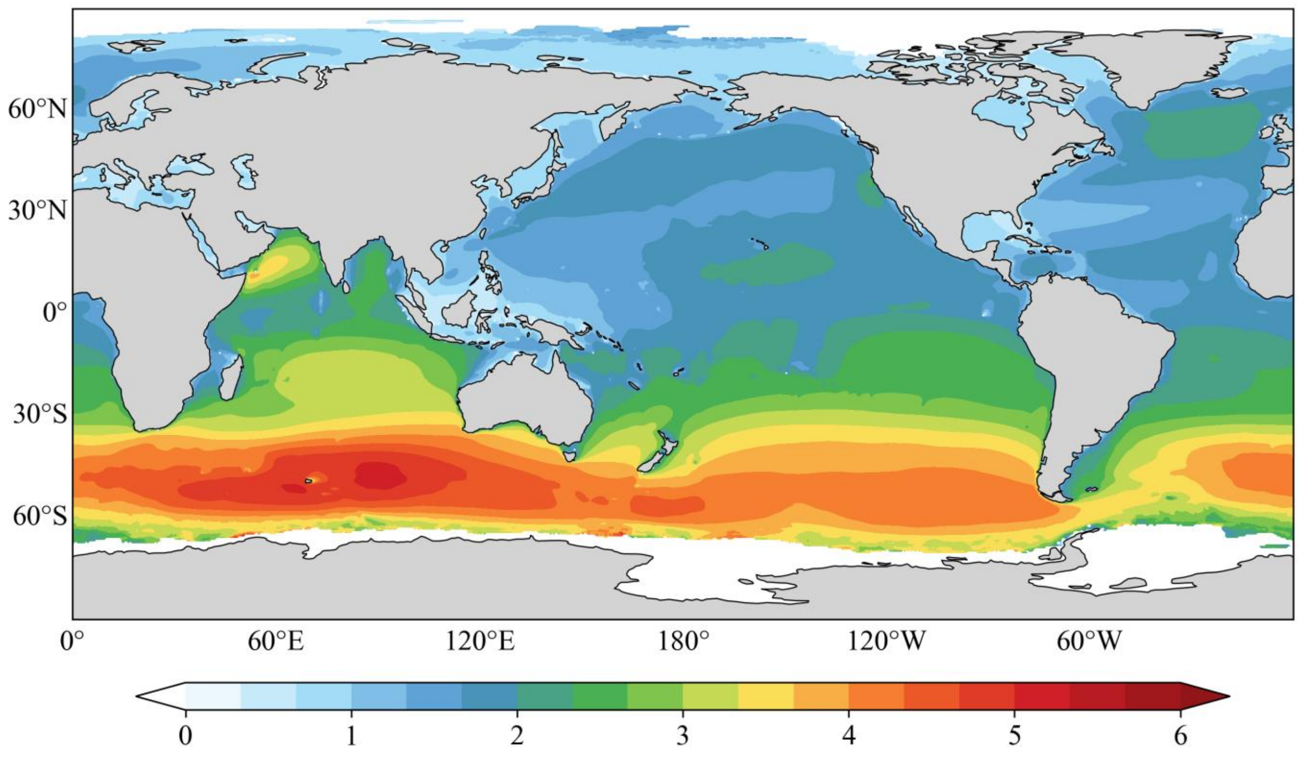

Figure 2: Summer climatology (June-July-August) of significant wave height (m) during 1993-2022 using the ERA5 reanalysis.

Providing observational backing for these numerical results, the hurricane and high-wind components of the CBLAST program proposed that the deficiencies in air-sea surface flux representations for high wind speed conditions are associated with three key factors: 1) the observations that surface momentum exchange coefficients increase with wind speed, are

https://doi.org/10.5194/essd-2026-476
Preprint. Discussion started: 31 August 2026

enhanced by fetch-limited waves or opposing swell, but level off or decrease above an extreme high wind threshold (> 45 m s^{-1}), especially in quadrants where swell has a significant downwind component; 2) that compensating mechanisms for enhanced surface air-sea fluxes over and above current parameterizations must exist for hurricane maintenance and growth above some high-wind threshold wind speed; and 3) that candidate mechanisms should include ocean wave interactions and sea spray. Surface winds in storms in the Southern Ocean can frequently reach hurricane strength, and the same uncertainties over the air-sea fluxes in hurricanes proposed by the hurricane and high-wind components of CBLAST also apply to storms in the Southern Ocean.

Beyond wind speed, the air-spray temperature difference (ΔT) is also a critical regulator of droplet thermodynamics(Mueller and Veron, 2014a; Veron, 2015). A positive ΔT ($T_{\text{spray}} > T_{\text{air}}$) directly enhances sensible heat release and accelerates latent heat transfer via elevated saturation vapor pressures at the droplet surface (Andreas, 1995). In the Southern Ocean, the coexistence of persistent high winds, extreme waves, and characteristically large air-sea temperature gradients creates a rich environment for large-scale spray production and enhanced thermodynamic transfer efficiency (Brumer et al., 2017; Meredith et al., 2019; Schulz et al., 2012). This combined dynamical and thermodynamical forcing makes the Southern Ocean one of the most active global hotspots for air-sea energy exchange (Bharti et al., 2019; Moura et al., 2025).

Recognizing the critical role of sea spray in modulating heat fluxes, extensive research has focused on parameterizing its effects. A widely recognized approach developed by Andreas et al. (2008, 2015) relies on a 50 μm' representative radius' to characterize the entire spray population, as droplets between 50–100 μm contribute most significantly to sensible and latent exchanges. Although computationally efficient, given that droplet thermal and evaporative responses are highly size-dependent (Andreas, 1995; Fairall et al., 1995; Veron, 2015) by neglecting the full size distribution this algorithm lacks the necessary granularity to capture diverse thermodynamic behaviours across the spray spectrum. This simplification inevitably leads to systematic biases, especially in the complex and variable sea states of the Southern Ocean. Additionally, the modulating influence of wave states on spray generation remains largely overlooked, introducing further uncertainties.

Although the importance of sea spray is widely recognized, it remains a missing process in current gridded products—whether from observations, reanalyses or satellite observations. Therefore, there is an urgent need for a dedicated spray-mediated heat flux dataset that explicitly accounts for both wave states and the complete size spectrum. In this study, we present a new 30-year (1993–2022) dataset of spray-mediated heat fluxes in the Southern Ocean, developed using a full spray microphysical model. This model combines the flux algorithm of Andreas et al. (2015) with the sea spray generation functions of Zhao et al. (2006, 2024). By jointly accounting for wind and wave state, our model allows for a more realistic representation of how sea spray generation is modulated by wave breaking, particularly under the characteristic long-fetch conditions of the Southern Ocean. For the first time, our dataset provides a quantitative assessment of spray-mediated contribution to the total air-sea energy exchange in the Southern Ocean, serving a critical foundation for examining the Southern Ocean's role in the global energy budget.

https://doi.org/10.5194/essd-2026-476
Preprint. Discussion started: 31 August 2026

2 Methods

2.1 Wave dependent sea spray generation function

As wind speed increases and waves intensify, an increasing number of sea spray droplets are generated within the air-sea boundary layer. Veron (2015) provide a systematic description of the microphysical mechanisms of spray generation: wave breaking is the direct physical source of sea spray and the generation process is jointly modulated by wave age, wave steepness, and water depth. Observations by Brumer et al. (2017) further showed that neglecting the influence of wave state can lead to systematic errors exceeding 20% in the estimation of spray-mediated heat fluxes. These results indicate that parameterizations based solely on near surface wind speed are insufficient to adequately represent sea spray droplet production. To address this limitation, we use a parameterization proposed by Zhao et al. (2006), which introduced the wind-sea Reynolds number R_B to characterize the coupled winds and waves and a spray droplet generation function that explicitly accounts for both factors. The wind-sea Reynolds number is calculated as follows:

$$R_\mathrm{B} = \frac{C_\mathrm{d} U_{10}^3 \beta_\mathrm{wave}}{g\nu} \qquad \beta_\mathrm{wave} = \frac{g P_\mathrm{wave}}{2\pi U_{10}} \tag{1}$$

$$\nu = 1.326 \times 10^{-5} \times \left(1 + 6.542 \times 10^{-3} T_\mathrm{s} + 8.301 \times 10^{-6} T_\mathrm{s}^2 - 4.84 \times 10^{-9} T_\mathrm{s}^3\right) \tag{2}$$

Here ν is the kinematic viscosity of air which is a function of sea surface temperature T_s (Eqs. 2). U_{10} is the 10-m wind speed, g denotes gravitational acceleration. β_wave represents the wave age of wind waves and is a function of peak wave period P_wave. The drag coefficient C_d is a linear function of U_{10}, given by $C_\mathrm{d} = 10^{-3} \times (0.8 + 0.065\, U_{10})$.

Based on this, the sea spray generation function (SSGF) is defined as a function of droplet initial radius r_0 and R_B, which can be written as:

$$dF/dr_0 = a R_\mathrm{B}^{1.5} r_0^{-b} \tag{3}$$

Here dF/dr_0 (expressed in $\mathrm{m^{-2}\ s^{-1}\ \mu m^{-1}}$) quantifies the production rate of spray droplets per unit sea surface area within a specific radius increment, a and b are constants depend on different spray sizes.

Spray-mediated heat fluxes are highly dependent on the droplet size spectrum, which governs droplet residence time scales (Andreas, 1990) and subsequent turbulent heat exchange (Andreas, 1992). Originally, the sea spray generation function (SSGF) proposed by Zhao et al. (2006) was formulated specifically for spume droplets generated by wave tearing. Based on empirical fits to laboratory data, this scheme partitioned the spume droplet spectrum into discrete radius (r_0) ranges, prescribing specific parameters (a and b) for intervals of $30 - 75\ \mu\mathrm{m}$, $75 - 200\ \mu\mathrm{m}$, or $200 - 500\ \mu\mathrm{m}$. However, as underscored by the evaporation parameterizations of (Kepert et al., 1999) and the Lagrangian stochastic simulations by (Mueller and Veron, 2014b), small sea spray droplets also play a crucial role in latent heat exchange. Their high concentration and negligible volume lead to rapid desiccation on sub-second timescales, facilitating a substantial transfer of latent heat to the atmosphere. To comprehensively capture their effects, Zhao et al. (2024) extended the SSGF framework by integrating micro-droplets generated from bubble bursting into the algorithm. By performing a least-squares regression on three classical whitecap and bubble-droplet models (Monahan et al., 1986; Woolf et al., 1988; Myrhaug et al., 2016), they

https://doi.org/10.5194/essd-2026-476
Preprint. Discussion started: 31 August 2026

analytically derived a new formula for these small droplets. To ensure physical and mathematical continuity across the spray spectrum, they consequently shifted the lower bound of the spume droplet regime from 30 μm to 20 μm. Building upon this, our calculation adopts this size-resolved SSGF but introduces a minor adjustment to the absolute lower limit. While Zhao et al. (2024) set the lower bound at 2 μm, we define it as 1.6 μm to perfectly align with the spray-mediated heat flux algorithm established by Andreas et al. (1992; 2015). Since the foundational bubble-mediated mechanisms fundamentally govern aerosol generation down to sub-micron scales, this slight threshold extension remains physically robust. Thus, our adopted dF/dr_0 is expressed as:

$$\frac{dF}{dr_0} = \begin{cases} 1.40 \times 10^{1} R_B^{1.5} r_0^{-3.5} & 1.6 < r_0 < 20\ \mu\text{m} \\ 7.84 \times 10^{-3} R_B^{1.5} r_0^{-1} & 20 < r_0 < 75\ \mu\text{m} \\ 1.40 \times 10^{1} R_B^{1.5} r_0^{-3} & 75 < r_0 < 200\ \mu\text{m} \\ 1.40 \times 10^{13} R_B^{1.5} r_0^{-8} & 200 < r_0 < 500\ \mu\text{m} \end{cases} \quad (4)$$

2.2 Spray-mediated heat fluxes

As discussed above, our full spray microphysical model considers spray droplets with various sizes. The inclusion of a population of very small spray droplets allows for the possibility that those droplets may evaporate entirely within the marine atmospheric boundary layer and have insufficient time to reach an equilibrium temperature. Thus, two different LHF formulations are applied, depending on whether the spray droplet falls back to sea surface or evaporates prior to re-entry. Specifically, for droplets with an initial radius r_0, the spray-induced LHF [$Q_L(r_0)$] and SHF [$Q_S(r_0)$] are expressed as:

$$Q_L(r_0) = \begin{cases} \rho_w L_v \left[1 - \left(\frac{r(\tau_f)}{r_0}\right)^3\right] \left(\frac{4\pi r_m^3}{3} \frac{dF}{dr_0}\right) & \tau_f < \tau_r \\ \rho_w L_v \left[1 - \left(\frac{r_{eq}}{r_0}\right)^3\right] \left(\frac{4\pi r_m^3}{3} \frac{dF}{dr_0}\right) & \tau_f > \tau_r \end{cases} \quad (5a)$$

$$Q_S(r_0) = \rho_w c_w (T_s - T_{eq}) \left(1 - e^{-\frac{\tau_f}{\tau_T}}\right) \left(\frac{4\pi r_m^3}{3} \frac{dF}{dr_0}\right) \quad (5b)$$

Here ρ_w and c_w denote the density of sea water and its specific heat, respectively, setting as 1000 kg m^{-3} and 4000 $\text{J kg}^{-1}\ \text{K}^{-1}$). The variable r_m is the initial radius of spray droplets in units of meter. L_v is the latent heat of vaporization, and can be expressed as follows:

$$L_v = \begin{cases} (25 - 0.02274\, T_{air}) \times 10^5 & T_s \geq 0°\text{C} \\ (28.34 - 0.00149\, T_{air}) \times 10^5 & T_s \geq 0°\text{C} \end{cases} \quad (6)$$

T_{air} is near-surface air temperature. T_s is sea surface temperature, also the droplets' initial temperature (T_{spray}). τ_T and τ_r are the e-folding time scales for spray droplets to reach the equilibrium status, and associated temperature of T_{eq} and radius of

https://doi.org/10.5194/essd-2026-476
Preprint. Discussion started: 31 August 2026

r_{eq} (detailed calculations for τ_T, τ_r, T_{eq} and r_{eq} can be found in the Supplementary Information). Thus, the residence time in the atmospheric boundary layer before falling back into sea (τ_f) can be parametrized as:

$$\tau_f = \frac{H_{\mathrm{s}}}{2u_f(r_0)} \tag{7}$$

Here $u_f(r_0)$ is the terminal fall speed of the spray droplets, and H_{s} is the significant wave height.

As shown by microphysical modelling in Andreas (1989) and Andreas et al. (1990), assuming constant ambient temperature and relative humidity, the radius *r* of the spray droplet, which evolves as a function of the time since its formation, can be calculated using the following Eq. (8), where we can calculate $r(\tau_f)$ by substituting t with τ_f.

$$\frac{r(t) - r_{\mathrm{eq}}}{r_0 - r_{\mathrm{eq}}} = \mathrm{e}^{-\frac{t}{\tau_r}} \tag{8}$$

Overall, in Eq. (5), for an individual droplet, $(4\pi r_{\mathrm{m}}^3/3)\, dF/dr_0$ is volume production rate of droplets with radius r_0, so $(4\pi\rho_{\mathrm{w}}/3)\left\{r_0^3 - \left[r\left(\tau_f\right)\right]^3\right\} dF/dr_0$ represents the water mass released by all droplets with initial radius r_0 during their residence time in the atmosphere; $\left(T_{\mathrm{s}} - T_{\mathrm{eq}}\right)[1 - \exp\left(-(\tau_f/\tau_T)\right)]$ is the temperature difference between droplets' formation and re-entry to the sea, driven by sensible heat exchange.

Finally, to obtain the total spray-mediated flux, Eq. (5a) and (5b) are integrated over the full range of droplet sizes.

$$H_{\mathrm{S,sp}} = \int_{1.6}^{500} Q_{\mathrm{S}}(r_0)\, dr_0 \tag{9a}$$

$$H_{\mathrm{L,sp}} = \int_{1.6}^{500} Q_{\mathrm{L}}(r_0)\, dr_0 \tag{9b}$$

$H_{\mathrm{S,sp}}$ and $H_{\mathrm{L,sp}}$ have units of heat flux (W m^{-2}). The flux integration is restricted to droplets with radii between 1.6 and 500 µm. Droplets smaller than 1.6 µm are excluded due to their negligible mass and minimal contribution to the total heat flux (Andreas, 1992), whereas those larger than 500 µm lack sufficient residence time for meaningful heat transfer (Veron, 2015).

2.3 Input Data

Several atmospheric and oceanic parameters are needed as inputs to calculate integrated spray-mediated fluxes across the full droplet spectrum, including 10-m wind speed (U_{10}), air temperature ($T_{2\mathrm{m}}$), relative humidity (RH), sea level pressure (SLP), significant wave height (H_{s}), peak wave period (P_{wave}), sea surface temperature (SST), and sea surface salinity (SSS). Various datasets are utilized to obtain these variables, which are summarized in Table 1. This study focused on the Southern Ocean, specifically the region south of 35°S.

https://doi.org/10.5194/essd-2026-476
Preprint. Discussion started: 31 August 2026

Open Access Earth System Science Data Discussions

Table 1 Summary of the variables used in this study.

Dataset	Variable Name	Unit	Resolution	Data Source
ERA5	sea surface temperature (SST)	℃	Monthly 0.25° × 0.25° 1993–2022	https://cds.climate.copernicus.eu/datasets/reanalysis-era5-single-levels-monthly-means
	sea level pressure (SLP)	hPa		
	significant wave height (H_s)	m		
	peak wave period (P_{wave})	m		
	2-m air temperature (T_{2m})	℃		
	2m dewpoint temperature (T_{2d})	℃		
	10-m Wind speed (U_{10})	m s^{-1}		
CMEMS	sea surface salinity	psu	Monthly 0.125° × 0.125° 1993–2022	https://data.marine.copernicus.eu/product/MULTIOBS_GLO_PHY_S_SURFACE_MYNRT_015_013
NSIDC	sea ice concentration	%	Monthly $25km \times 25km$ 1993–2022	https://nsidc.org/data/nsidc-0079/versions/4

2.3.1 ERA5 Data

SST, SLP, H_s, P_{wave}, T_{2m}, U_{10} and 2-m dewpoint temperature (T_{2d}) are obtained from the ERA5 reanalysis dataset (Hersbach, 2023), produced by the European Centre for Medium-Range Weather Forecasts (ECMWF). Relative humidity is calculated using T_{2m} and T_{2d}. The dataset is publicly available through the Copernicus Climate Change Service (C3S).

2.3.2 CMEMS Salinity Data

Monthly sea surface salinity (SSS) fields are obtained from the multi-observation global product provided by the Copernicus Marine Service (CMEMS). This product reconstructs global SSS by combining in-situ measurements from the CORA database with satellite observations from SMOS, SMAP, and Aquarius, using a multi-dimensional optimal interpolation approach (Droghei et al., 2016). To ensure consistency with other variables, the SSS fields were spatially interpolated onto the ERA5 grid prior to the analysis.

2.3.3 NSIDC Sea ice concentration Data

Monthly mean sea ice concentration (SIC) data are obtained from the National Snow and Ice Data Centre (NSIDC), derived from Nimbus-7 SMMR and DMSP SSM/I–SSMIS using the Bootstrap algorithm, Version 4 product (Comiso, 2023). The

https://doi.org/10.5194/essd-2026-476
Preprint. Discussion started: 31 August 2026

dataset has a spatial resolution of 25 km on a polar stereographic grid, which is specifically designed for polar regions and minimizes spatial distortion at high latitudes. For consistency with other variables, the SIC data are also interpolated to the ERA5 grid. We also construct a sea ice mask for the study region, ensuring that spray-mediated flux calculations are restricted to open-water conditions.

2.4 Climate Indices

To investigate the relationship between spray-mediated turbulent heat flux (THF) and large-scale climate variability, monthly climate indices were utilized in this study. These indices include the El Niño-Southern Oscillation (Niño 3.4), Southern Annular Mode (SAM), Indian Ocean Dipole (IOD), Amundsen Sea Low (ASL), and Zonal Wave 3 (ZW3). All these climate index datasets were obtained from the NOAA Physical Sciences Laboratory (PSL) climate indices repository (https://psl.noaa.gov/data/climateindices/list/). These standardized indices provide a consistent and reliable basis for examining the spatial correlations with turbulent heat fluxes across the Southern Ocean.

3 Data Records

The spray-mediated heat flux dataset is provided in NetCDF-4 format and spans the period from January 1993 to December 2022. It has a monthly temporal resolution and a spatial resolution of 0.25°, covering the Southern Ocean (south of 35°S). The dataset contains two variables: QL_S_ALL ($H_{L,sp}$) and QS_S_ALL ($H_{S,sp}$). The former is the total spray-induced latent heat flux, while the latter is the total spray-induced sensible heat flux. Both variables are defined on a three-dimensional grid with dimensions of time × latitude × longitude, and their units are W m^{-2}. In our study, positive flux means heat transfer from ocean to the atmosphere. As noted above, a grid cell is considered ice-covered when sea ice concentration exceeds 15%, and these grid points are excluded from the spray flux calculations. It should be noted that this dataset exclusively represents the spray-mediated components of the heat fluxes. Users intending to derive the total air–sea heat fluxes should supplement these data with the surface heat fluxes from existing atmospheric models.

4 Validation

4.1 Climatology of spray-mediated heat fluxes

4.1.1 Annual mean

Figure 3 presents the climatology of spray-mediated heat fluxes over the Southern Ocean averaged during 1993–2022. The LHF dominates the total spray-mediated energy exchange (Fig. 3a vs. Fig. 3b). The LHF varies from 0.02 to 38.1 W m^{-2}, with an average of 12.3 W m^{-2}, which is comparable to, but is relatively smaller than, that calculated from the bulk flux algorithm (Liu et al., 2011; Song et al., 2022). It exhibits a pronounced circumpolar band of large positive values centred near 50°S (Fig. 3a). Geographically, the largest LHF is concentrated within the Indian Ocean sector, particularly between 60°E and 120°E, where the averaged LHF is approximately 25.5 W m^{-2} (red box in Fig. 3a). Beyond this region, the LHF gradually decreases on both sides, with a faster decline westward than eastward. As demonstrated in previous studies (e.g., Liu et al., 2011) the LHF calculated based on the bulk flux algorithm has maxima localized over the Western Boundary Current (WBC) regions (e.g., the East Australian Current), where large air-sea temperature differences and strong offshore winds, especially in austral winter, lead to substantial latent heat release. In contrast, the maximum spray-mediated LHF is observed along the primary westerly storm tracks (Eichler and Gottschalck, 2013; Priestley et al., 2020), characterized by strong winds and large waves. This spatial discrepancy in peak values implies that these two LHF calculations are governed by different physical processes, and further highlights that sea spray processes are inadequately represented in current air-sea flux datasets. As shown in Fig. 4, the spatial pattern of the LHF standard deviation is consistent with its climatology, although the band of large value is latitudinally broader. This suggests that large variability of the spray-mediated LHF is mainly driven by the frequent passage of storm systems in the Southern Ocean.

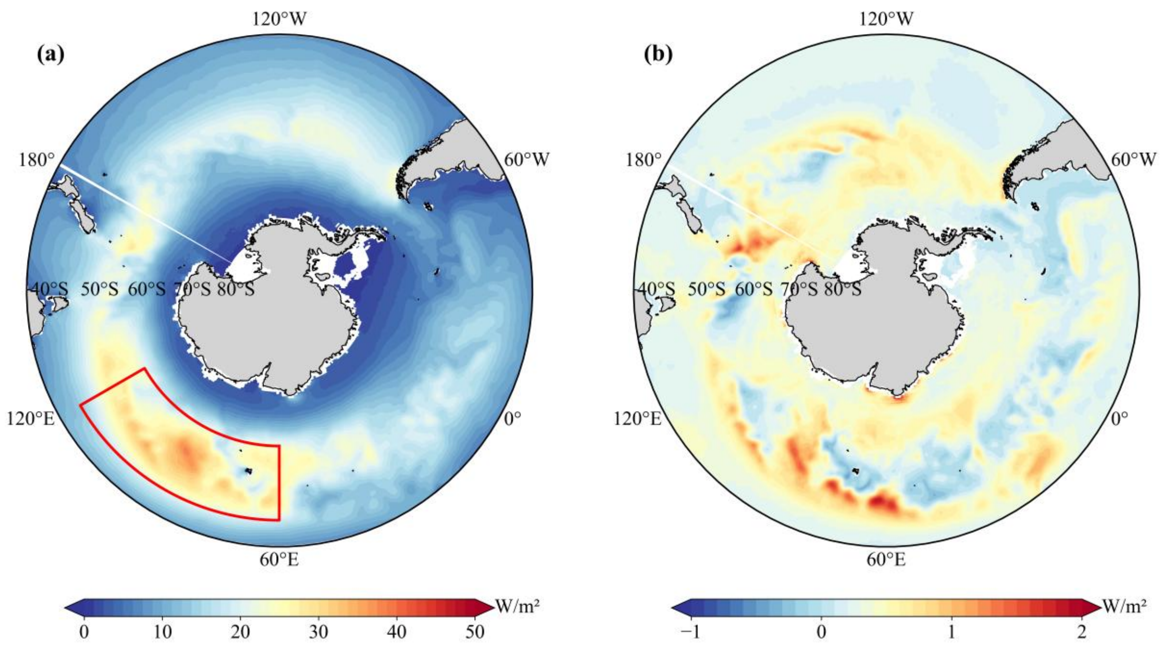

Figure 3: Spatial distribution of the annual mean (a) spray-mediated latent heat flux and (b) sensible heat flux during 1993 to 2022. Blank areas indicate regions covered by sea ice (SIC>0.15). The heat flux in positive upward.

Compared to the LHF, the SHF is an order smaller in magnitude and displays more spatial heterogeneity. It ranges from −0.5 to 1.8 W m^{-2}, with a mean value of 0.4 W m^{-2}. Unlike the LHF, its climatological distribution (Fig. 3b) does not exhibit a distinct circumpolar band of high values. It is more characterized by alternating positive and negative values in the circumpolar regions. Such alternating features are evident in the South Indian and South Pacific sectors, whereas the Atlantic sector is predominantly characterized by small values. The standard deviation of SHF (Fig. 4b) also shows large variability over the regions with large positive values in Fig. 3b. This strong regional variability suggests that the spray-mediated sensible heat flux may be highly sensitive to synoptic-scale disturbances, such as cyclones and fronts (Ogle et al., 2018; Perrie et al., 2005).

These distinct spatial structures—where LHF is primarily governed by dynamical forcing (e.g., wind and wave conditions) along storm tracks, while SHF is tightly modulated by local thermodynamic gradients—exhibit strong physical consistency with the background climatological state of the Southern Ocean. This coherence provides support for the reliability of our full spray microphysical model in representing large-scale spray production and associated heat exchanges under the coexistence of high winds, large waves, and large air-sea temperature gradients.

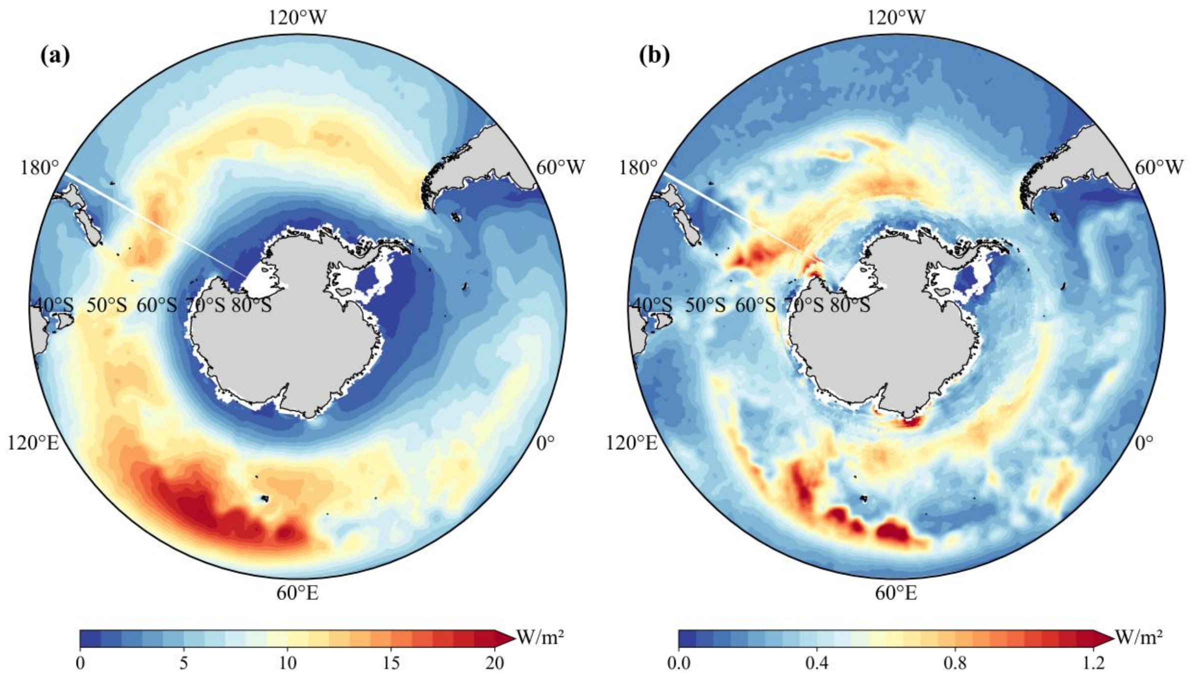

Figure 4: Standard deviation of spray-mediated (a) latent heat flux and (b) sensible heat flux for the period 1993–2022. Sea ice covered regions (SIC > 0.15) are masked.

4.1.2 Seasonal variability

Modulated by wind-wave states, spray-mediated heat fluxes exhibit pronounced seasonal variability. Figs. 5 and 6 illustrate the spatial distributions of spray-induced LHF and SHF over the Southern Ocean for different seasons. Overall, both fluxes reach their minimum during the austral summer (DJF) and their peak in the austral winter (JJA). This seasonal pattern is consistent with seasonal variations of the Southern Hemisphere westerlies, indicating that spray-mediated heat fluxes are primarily governed by the seasonal migration of the westerly jet and associated storm tracks, which generate intense winds and large waves. As shown in Fig. 5, LHF ranges from 0 to 53.6 W m^{-2}. Despite different magnitude for the four seasons, spray consistently releases latent heat into the atmosphere. A circumpolar band of high values is evident around ~50°S, with the strongest signals located in the western Indian Ocean sector. The LHF is weakest during DJF, with a regional mean of

https://doi.org/10.5194/essd-2026-476
Preprint. Discussion started: 31 August 2026

Open Access Earth System Science Data Discussions

approximately 7.2 W m^{-2}. Driven by the intensification of winds, it gradually strengthens through MAM and reaches its maximum in JJA. During the peak season, the spray-mediated LHF is substantially larger than that estimated by bulk flux algorithms in the circumpolar region.

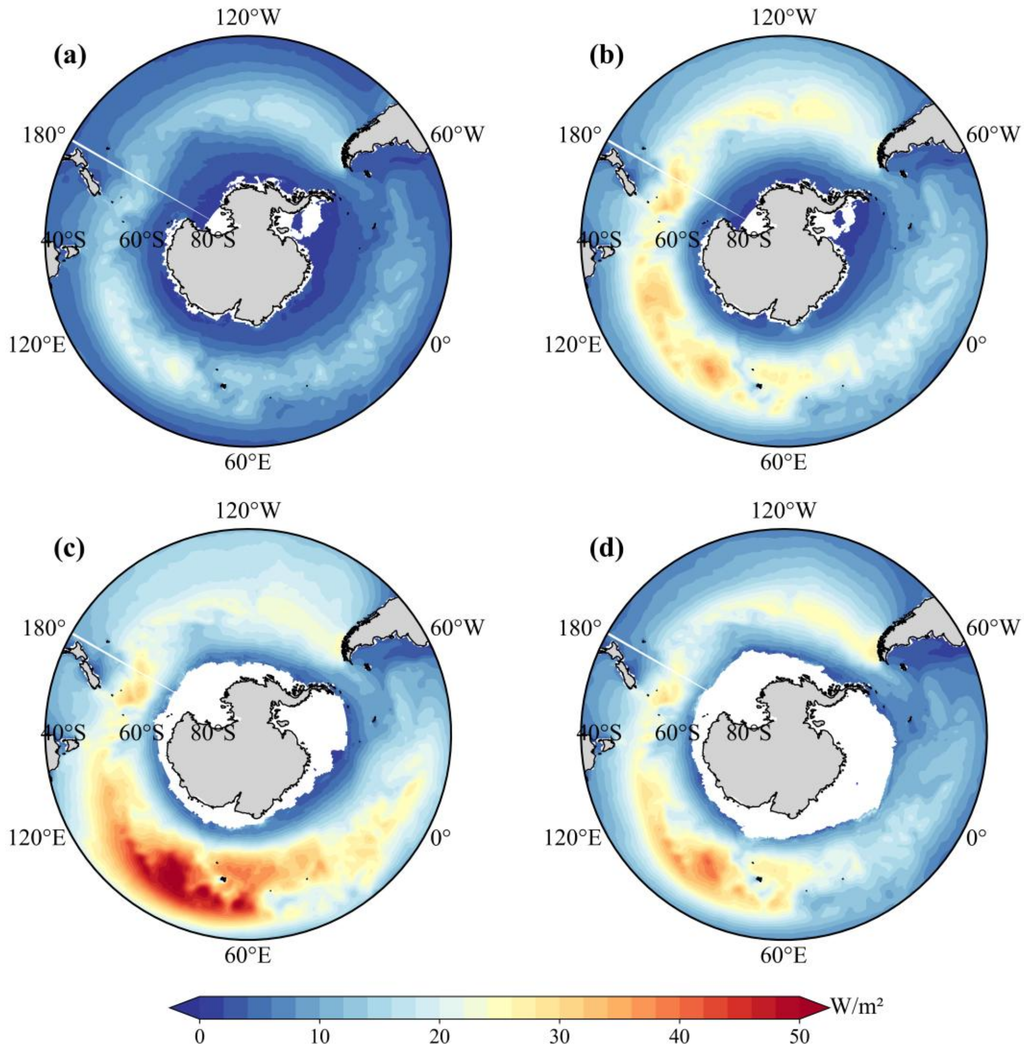

Figure 5: Seasonal spatial distribution of spray-mediated latent heat flux for the period 1993-2022 (positive upward). (a) December-January-February, (b) March-April-May, (c) June-July-August, (d) September-October-November. Blank areas indicate regions covered by sea ice.

The seasonal evolution of SHF (Fig. 6) broadly mirrors that of LHF. Unlike LHF, spray-mediated SHF is primarily governed by local air-spray temperature gradients (Andreas, 1992), it exhibits more pronounced spatial heterogeneity. During the austral summer, enhanced incoming solar radiation and surface warming substantially reduce the air-sea temperature difference, thereby suppressing sensible heat exchange between droplets and atmosphere (since droplets' initial temperature = SST). As a result, SHF reaches its annual minimum, ranging approximately from −0.5 to 0.5 W m^{-2}, with a regional mean

https://doi.org/10.5194/essd-2026-476
Preprint. Discussion started: 31 August 2026

of only 0.06 W m^{-2}. As the season transitions to austral winter, the westerlies intensify significantly, and strong wind-wave conditions generate abundant sea spray. At the same time, the frequent passage of storm systems drives alternating warm and cold advection (Hoskins and Hodges, 2005). This markedly increases the SHF magnitude, with peak value exceeding 6.3 W m^{-2}, accompanied by increased spatial heterogeneity. Notably, during JJA, pronounced positive SHF values extend southward beyond 60°S, well beyond the core region of the westerly jet. This spatial expansion suggests that, large air-sea temperature differences associated with high-latitude cold-air outbreaks may also contribute to the enhancement of sensible heat transfer.

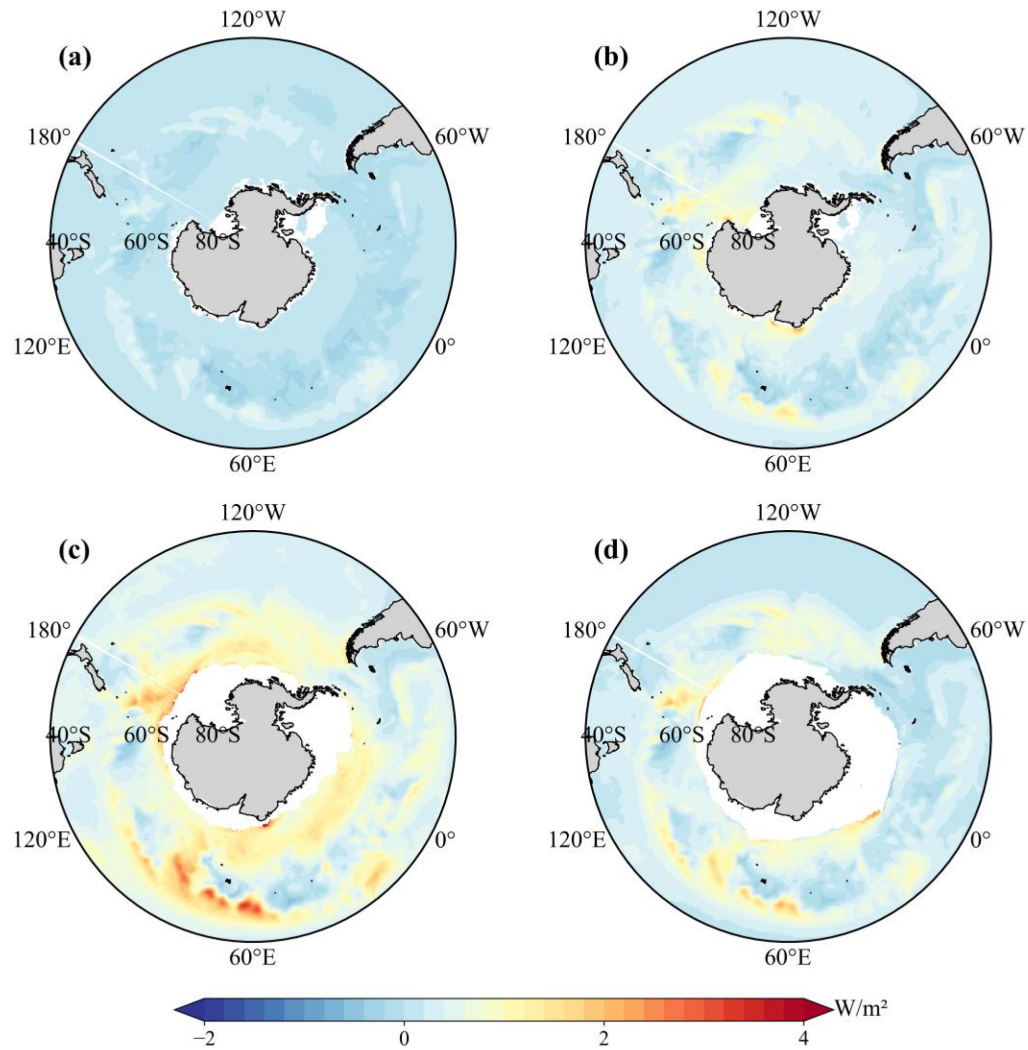

Figure 6: Same as Figure 5, but for spray-mediated sensible heat flux.

https://doi.org/10.5194/essd-2026-476
Preprint. Discussion started: 31 August 2026

4.2 Validation of the data using an aircraft-based dataset

Direct observations of turbulent heat fluxes (THF) during high windspeed conditions are scarce. To validate our full spray microphysical model, we used an aircraft-based observational dataset collected by Petersen and Renfrew (2009) over the Irminger and Iceland Seas in the NE Atlantic. The observations in this dataset were conducted 100–400 km offshore, largely outside the continental shelf. During this period, cold-air outbreaks drove prevailing north-to-northeasterly winds with speeds predominantly ranging from 10 to 25 m s^{-1} (Renfrew et al., 2009a).Under these conditions, significant wave heights reached up to ~10 m in some cases (Renfrew et al., 2009b), providing wind and wave regimes similar to the Southern Ocean conditions targeted in our study. The dataset provides direct flux measurements obtained from the eddy covariance method (hereafter 'Observation' in Fig. 7), along with fluxes estimated using a bulk flux parameterization (after Smith, 1988).

As shown in Fig. 7a, the traditional bulk flux method, which does not consider sea-spray processes, exhibits a pronounced underestimation for large heat fluxes (> 500 W m^{-2}). This bias becomes particularly clear as wind speeds exceed 20 m s^{-1}. Fig. 7b displays the total THF after combining the estimate by the bulk method with the spray-mediated heat fluxes calculated by our full spray microphysical model, we can see that incorporating sea-spray processes largely corrects the systematic low bias. However, the high-wind sample size is relatively limited, with only 151 data points exceeding 15 m s^{-1}, and there still have some inherent uncertainties in the parameters employed in our full spray microphysical model. Although our results indicate that the spray microphysical model provides a significant correction to the air-sea surface flux algorithm, caution is required in determining whether these results can represent the conditions of the Southern Ocean region, given the factors mentioned above.

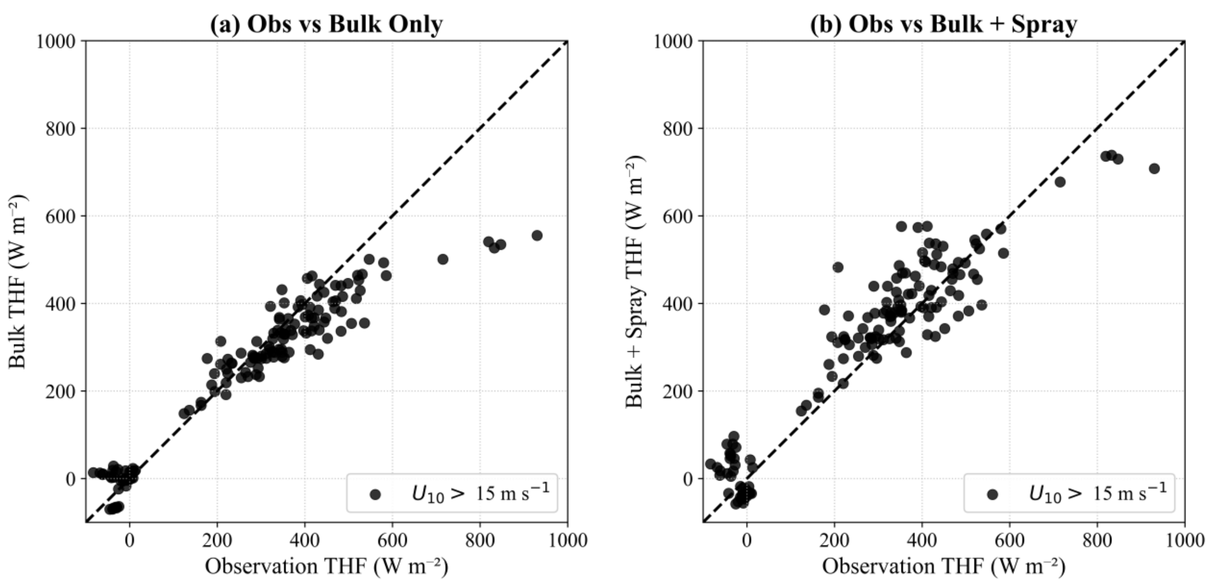

Figure 7: Comparison of observed and estimated turbulent heat fluxes (THF) under high wind conditions (U_{10}>15 m s^{-1}). The x-axis represents the observed THF, and the y-axis represents the estimated THF. (a) THF estimated using the bulk method (provided in the observational dataset, following Smith, 1988); (b) Total THF incorporating the spray heat flux calculated by our full spray microphysical model.

https://doi.org/10.5194/essd-2026-476
Preprint. Discussion started: 31 August 2026

4.3 Examination of the data in an extreme cyclone

As noted above, spray-mediated turbulent heat fluxes are substantially enhanced under conditions of strong winds, high waves, and large air-spray temperature differences. To validate the performance of the full spray microphysical model, a case study based on a historical extreme weather event is conducted. On 16 October 2022, a record-breaking extratropical cyclone (hereafter EC2022) occurred over the southeastern Pacific sector of the Southern Ocean (Hewson, 2023). During this event, extreme surface wind speeds and high waves provided favourable conditions for the generation of abundant sea spray and its subsequent impact on air-sea heat fluxes. Under these extreme conditions, conventional interfacial flux parameterizations typically exhibit significant deficiencies.

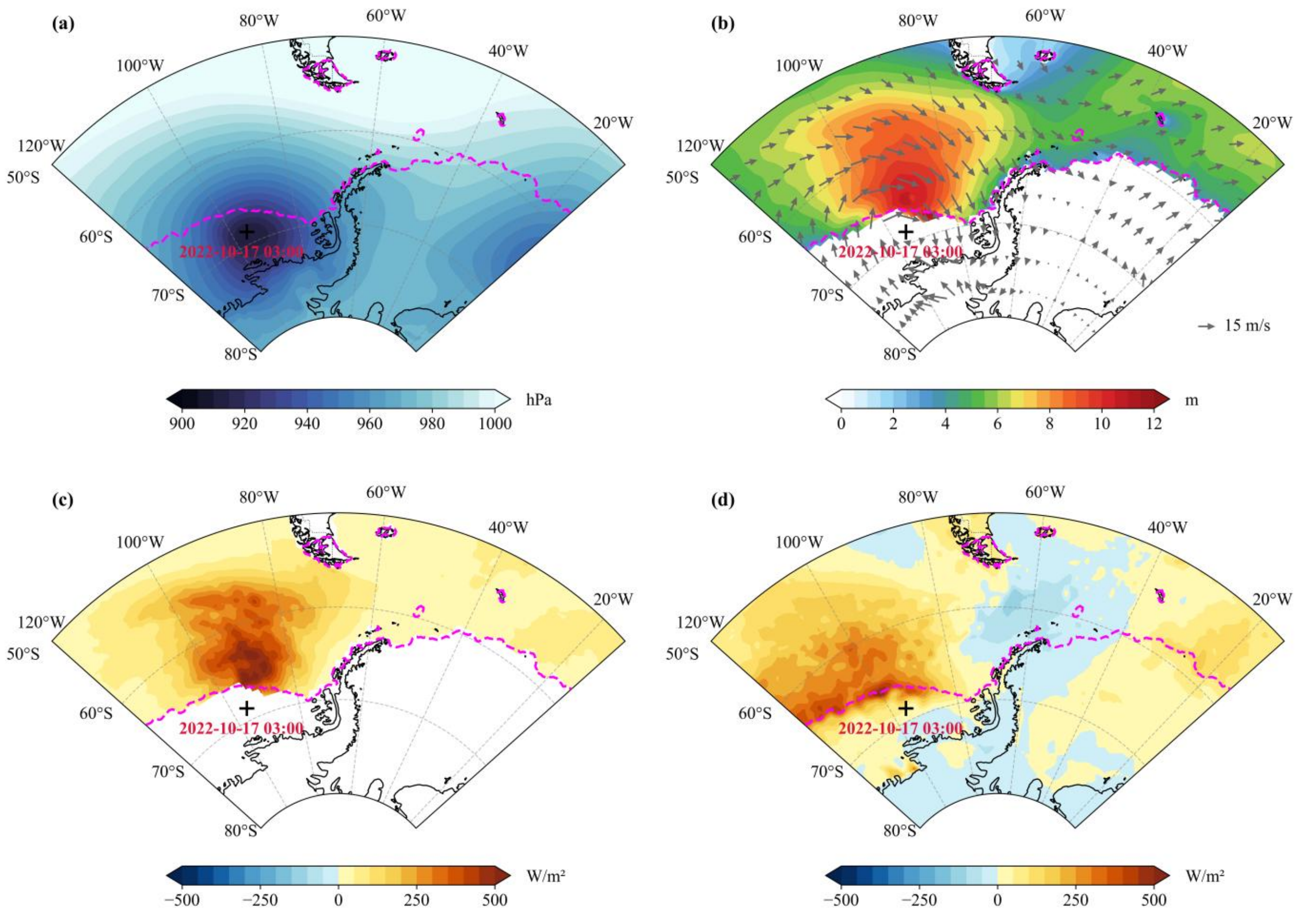

Figure 8: Case study of the record strong cyclone in the Southern Ocean on 17 October 2022. (a) Sea level pressure; (b) Significant wave height (shading) and 10-m wind speed (arrows); (c) Spray-mediated turbulent heat flux; (d) ERA5 turbulent heat flux. The cross (+) marks the cyclone center, and the pink dashed line denotes the 0.15 sea-ice concentration contour.

We focus the analysis on the storm's peak intensity at 03:00 UTC on 17 October 2022. Fig. 8 presents the background fields and the spatial distribution of turbulent heat fluxes during the peak intensity of EC2022. As shown in Fig. 8a, the centre of the cyclone is located east of the Antarctic Peninsula and its central sea-level pressure reached a record low of ~900 hPa

https://doi.org/10.5194/essd-2026-476
Preprint. Discussion started: 31 August 2026

during its lifecycle. The intense westerly winds reaching ~30 m s^{-1} occurred north of the cyclone centre (Fig. 8b), which is driven by the superposition of the cyclonic circulation and prevailing westerlies. Forced by these strong winds, the associated significant wave height in this region reaches approximately 12 m. Under these extreme conditions, the ERA5 interfacial turbulent heat flux (Fig. 8d), which is calculated using the bulk flux algorithm, exhibits elevated values in the northwestern sector, peaking at 542 W m^{-2}. However, its spatial distribution is relatively diffuse, lacking a well-defined vortex structure, with maximum values concentrated near the sea-ice edge. This feature likely results from strong post-cyclone winds fracturing thin sea ice, exposing relatively warmer, previously insulated seawater. The resulting amplification of air-sea temperature difference enhances sensible heat release from ocean to the ambient air, while the exposed open water increases near-surface humidity, leading to enhanced latent heat transfer. These combined effects elevate the ERA5 turbulent heat flux near the sea-ice boundary. In contrast, the high-flux region derived from the full spray microphysical model (Fig. 8c) shifts toward the northern side of the cyclone. The maximum value reaches 548 W m^{-2}, which is comparable to the ERA5 flux. Furthermore, the spatial distribution of spray-mediated turbulent heat flux aligns strongly with the significant wave height, exhibiting a vortex-like structure. This coherence suggests that spray processes play a significant role in fuelling the cyclone during its development. After incorporating the spray contribution, the total turbulent heat flux increases substantially, with a maximum of up to 853 W m^{-2}—one to two times higher than the ERA5 estimate. This discrepancy indicates that, under extreme sea states, spray-induced fluxes constitute a considerable fraction of the total turbulent heat flux. Relying solely on conventional bulk flux algorithm leads to a significant underestimation of air–sea heat exchange, which is not capable to allow the development of the record cyclone. Thus, this case study demonstrates that our dataset effectively captures the impact of sea spray on air-sea heat fluxes, particularly under strong wind and huge wave conditions, where sea spray plays a critical modifying role in the development of strong cyclones in the Southern Ocean.

4.4 Relationship between spray-mediated heat fluxes and modes of climate variability

To investigate the relationship between spray-mediated turbulent heat flux (THF) and large-scale climate variability, Fig. 9 presents the spatial correlation between THF and various climate indices. The selected indices include: El Niño–Southern Oscillation (Niño 3.4), Southern Annular Mode (SAM), Indian Ocean Dipole (IOD), Amundsen Sea Low (ASL), and Zonal Wave 3 (ZW3).

Among all climate indices, SAM and ASL have the most prominent relationships with spray-mediated heat fluxes. The THF associated with SAM displays a typical annular pattern. The 50°S–60°S latitudinal band is dominated by significant positive correlations ($r > 0.5$), peaking in the Indian Ocean sector ($r \approx 0.6$). In the Pacific sector, this positive correlation region extends northward to approximately 40°S. Conversely, the mid-to-low latitude oceans between 35°S and 45°S exhibit significant negative correlations (ranging from −0.5 to −0.4), especially in the Indian and Pacific Ocean sectors. The THF linked to ASL also presents an annular structure, but its spatial phase is largely opposite to that of SAM. Previous studies have shown that a positive SAM strengthens circumpolar westerlies, which results in a deepening of ASL (Hosking et al.,

https://doi.org/10.5194/essd-2026-476
Preprint. Discussion started: 31 August 2026

2013; Raphael et al., 2016). Furthermore, unlike the SAM, the ASL pattern displays its broadest and strongest negative signal (reaching −0.8 locally) in the Pacific sector, extending northward to 40°S.

Unlike the annular patterns of SAM and ASL, the THF associated with Niño 3.4 and IOD exhibit obvious regionality. Niño 3.4 shows localized significant negative correlations between 140°W and 60°W (ranging from −0.5 to −0.3), alongside significant positive correlations ($r \approx 0.4$) south of Australia and New Zealand. The IOD displays a similar spatial distribution, but with a smaller region of negative correlation in the Pacific sector. Additionally, the ZW3 index presents a typical zonal wave-three structure with alternating phases. Significant negative correlations are primarily located in the Pacific sector and the southern Indian Ocean, while significant positive correlations occupy the adjacent regions, specifically west of South America and south of Australia and New Zealand.

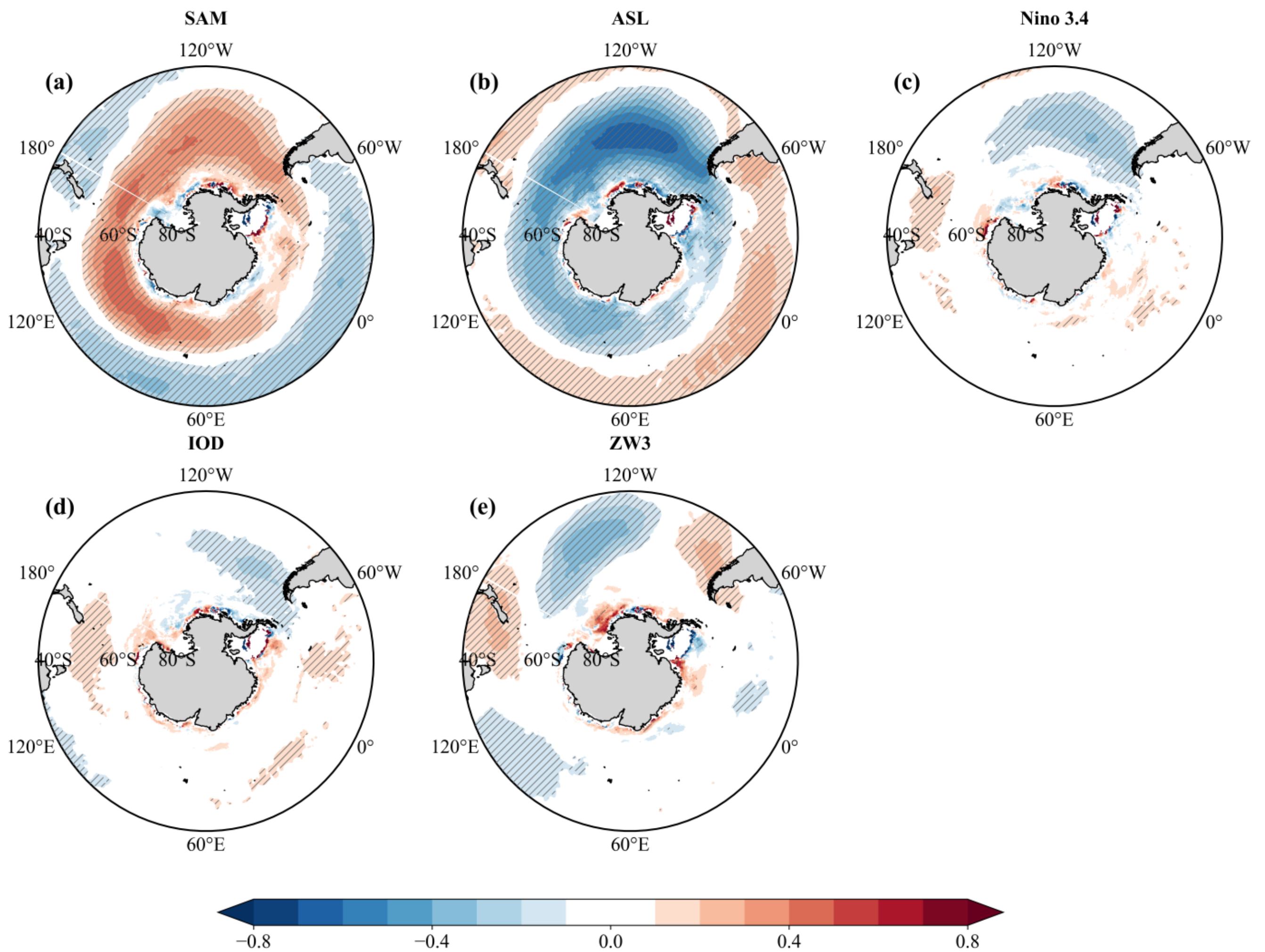

Figure 9: Correlation coefficients between spray-mediated turbulent heat flux and selected climate indices. Hatched areas indicate statistical significance at the 95% confidence level. Abbreviations: SAM, Southern Annular Mode; ASL, Amundsen Sea Low; IOD, Indian Ocean Dipole; ZW3, Zonal Wave 3 (phase index).

https://doi.org/10.5194/essd-2026-476
Preprint. Discussion started: 31 August 2026

Open Access Earth System Science Data Discussions

Appendix A

The bulk spray-mediated flux algorithm was introduced in detail by Andreas et al. (2008, 2015), and the related calculations of variables were provided by Andreas (1989, 1992) and Andreas et al. (1990, 1995).

The equilibrium radius r_{eq} is defined as the state at which the saturation vapor pressure at the droplet surface (modified by both curvature and salinity effects), exactly equals the ambient water vapor pressure. Under this condition, the droplet neither evaporates nor grows, and its radius remains stable. Determination of the equilibrium radius r_{eq} therefore reduces to solving the steady-state vapor pressure balance, commonly referred to as the Köhler equation. The governing equation is defined as follows:

$$G(r_{\mathrm{eq}}) = f - 1 - \left(\frac{\Phi_{\mathrm{k}}}{r_{\mathrm{eq}}} - \frac{\Phi_{\mathrm{s}}}{r_{\mathrm{eq}}^3 - r_{\mathrm{d}}^3}\right) = 0 \qquad (S1)$$

where Φ_{k} and Φ_{s} represent the curvature and solute effect, respectively. f is the fractional relative humidity. r_{d} is the dry salt core radius which refers to the radius of the residual solid sea salt particle remaining after complete evaporation of all liquid water in the droplet. This radius determines the total solute mass (m_{s}) contained within the droplet and remains conserved throughout the entire evaporation process. Since r_{eq} is implicit in the non-linear Köhler equation, the subroutine employs the Newton-Raphson method to converge on the solution. The iterative step is expressed as:

$$r_{n+1} = r_n - \frac{G(r_n)}{G'(r_n)} \qquad (S2)$$

The iteration terminates when the relative change in radius falls below a convergence threshold of 0.001.

To account for the latent heat cooling during evaporation, the droplet equilibrium temperature T_{eq} is determined based on the thermodynamic framework of Kepert (1996) with the modifications proposed by Andreas (2005). The equilibrium state is reached when the sensible heat flux from the environment is perfectly balanced by the latent heat flux associated with the phase change at the droplet surface. Following a second-order Taylor expansion of the heat and mass transfer equations, the temperature depression $\Delta T = T_{\mathrm{eq}} - T_{\mathrm{air}}$ is solved via a quadratic algebraic equation:

$$A\Delta T^2 + B\Delta T + C = 0 \qquad (S3)$$

where the coefficients are defined to represent specific physical feedback mechanisms.

C is the Thermodynamic Forcing Term which represents the moisture deficit between the ambient relative humidity (f) and the equilibrium vapor pressure at the droplet surface, modified by curvature and solute effects (e^y):

$$C = -\beta'[f - \mathrm{e}^y] \qquad (S4)$$

B is the Linear Feedback Coefficient and it characterizes the linear response of the heat balance to temperature changes, incorporating the coupling between latent heat and thermal conduction:

$$B = 1 + \frac{\beta'}{T_{\mathrm{air}}}(\alpha' - 1)\mathrm{e}^y \qquad (S5)$$

https://doi.org/10.5194/essd-2026-476
Preprint. Discussion started: 31 August 2026

A is the Non-linear Correction Term and this term accounts for the non-linear relationship between saturation vapor pressure and temperature, as parameterized by the Buck (1981) equation:

$$A = \frac{\beta'}{T_{\mathrm{air}}^2}\left[\frac{\alpha'^2}{2} - \alpha'\left(\frac{2T_{\mathrm{air}} + \mathrm{b} - 273.15}{T_{\mathrm{air}} + \mathrm{b} - 273.15}\right) + 1\right] e^{y} \qquad (S6)$$

The auxiliary dimensionless parameters α', β' and y are defined as follows:

$$\alpha' = \frac{\mathrm{ab}T_{\mathrm{air}}}{(\mathrm{b} + T_{\mathrm{air}} - 273.15)^2} \qquad (S7a)$$

$$\beta' = \frac{E_{\mathrm{sat}}(T_{\mathrm{air}})L_{\mathrm{v}}M_{\mathrm{w}}D_{\mathrm{wp}}}{T_{\mathrm{air}}\mathrm{R}\kappa_p} \qquad (S7b)$$

$$y = \frac{2M_{\mathrm{w}}\sigma_{\mathrm{s}}}{\mathrm{R}T_{\mathrm{air}}\rho_{\mathrm{w}}r} - \frac{\gamma'\varnothing_{\mathrm{s}}m_{\mathrm{s}}\dfrac{M_{\mathrm{w}}}{M_{\mathrm{s}}}}{\left(\dfrac{4\pi\rho_{\mathrm{s}}r^3}{3}\right) - m_{\mathrm{s}}} \qquad (S7c)$$

where $a = 17.502$ and $b = 240.97$ are constant coefficients for the saturation vapor pressure over water. Other parameters are shown in the following table.

Variable	Description	Variable	Description
M_{s}	Molecular weight of salt	$E_{\mathrm{sat}}(T_{\mathrm{air}})$	Saturation vapor pressure at T_{air}
M_{w}	Molecular weight of water	D_{wp}	Modified molecular diffusivity of water vapor in air
m_{s}	The mass of salt in the droplet	κ_{p}	Modified thermal conductivity of air
R	The universal gas constant	ρ_{w}	Density of sea water
σ_{s}	Surface Tension of a flat surface	r	Droplet radius
γ'	Number of ions produced upon dissociation of a salt molecule.	$\varnothing_{\mathrm{s}}$	Particle osmotic coefficient
ρ_{s}	Density of dry sea salt	L_{v}	Latent heat of vaporization

For the computation of the e-folding time scale τ_r and τ_T, we use the following equation:

$$\tau_r = \frac{-\dfrac{dr}{dt} - \sqrt{3\;\dfrac{dr}{dt}^{2} - 2\left(r_0 - r_{\mathrm{eq}}\right)\dfrac{d^2r}{dt^2}}}{\dfrac{d^2r}{dt^2} - \dfrac{\dfrac{dr}{dt}^{2}}{r_0 - r_{\mathrm{eq}}}} \qquad (S8a)$$

$$\tau_T = \frac{r_{\mathrm{m}^2}\rho_{\mathrm{sol}}c_{pw}}{3\left[\kappa_p + L_{\mathrm{v}}D_{\mathrm{wp}}\left(\dfrac{d_{\rho_{\mathrm{v}},\mathrm{sat}}}{dT}\right)\right]} \qquad (S8b)$$

Here, ρ_{s} and c_{pw} are the density and specific heat capacity of droplet solution, respectively. $d\rho_{\mathrm{v,sat}}/dT$ is the temperature derivative of the saturation vapor density.

https://doi.org/10.5194/essd-2026-476
Preprint. Discussion started: 31 August 2026

Code and data availability

The code used to generate the dataset and the final version dataset are available at https://doi.org/10.5281/zenodo.19351195 (Yi et al., 2026). Users can effortlessly process this dataset using mainstream scientific data analysis software. Python implementations can parse the files and retrieve internal variables using the xarray ("open_dataset") or netCDF4 ("Dataset") routines. Similarly, the data remains fully compatible with NCL (NCAR Command Language), where the "addfile" function enables direct access to all variables and attributes.

Author contributions

Conceptualization and methodology, J.L. and A.Y.; Software, data curation, and visualization, A.Y. and C.Y.; Formal analysis and investigation, A.Y. and J. L.; Validation, A.Y., J.L., I.R.; Resources and funding acquisition, J.L.; Writing and editing, A.Y., J.L., I.R., C.D. Q.Y. and X.S.; Supervision and project administration, J.L. All authors contributed to the discussion of the results.

Competing interests

The contact author has declared that neither of the authors has any competing interests.

Disclaimer

Copernicus Publications remains neutral with regard to jurisdictional claims made in the text, published maps, institutional affiliations, or any other geographical representation in this paper. While Copernicus Publications makes every effort to include appropriate place names, the final responsibility lies with the authors. Views expressed in the text are those of the authors and do not necessarily reflect the views of the publisher.

Acknowledgements

We acknowledge the European Centre for Medium-Range Weather Forecasts (ECMWF) for providing the ERA5 reanalysis data through the Copernicus Climate Change Service (C3S). We also thank the Copernicus Marine Service (CMEMS) for the sea surface salinity data, the National Snow and Ice Data Centre (NSIDC) for the sea ice concentration data, and the developers of the J-OFURO3 dataset and CERES project for making their products publicly available. Finally, this work greatly benefited from open-source software ecosystems and public data repositories that support transparent and reproducible climate data research.

Financial support

This research is supported by the National Key R&D Program of China (2024YFF0506600) and the Southern Marine Science and Engineering Guangdong Laboratory (Zhuhai) (SML2024SP023).

Review statement

The review statement will be added by Copernicus Publications listing the handling editor as well as all contributing referees according to their status anonymous or identified.

References

Andreas, E. L.: Thermal and Size Evolution of Sea Spray Droplets, 1989.

Andreas, E. L.: Time constants for the evolution of sea spray droplets, Tellus B: Chemical and Physical Meteorology, 42, 481–497, https://doi.org/10.3402/tellusb.v42i5.15241, 1990.

Andreas, E. L.: Sea spray and the turbulent air-sea heat fluxes, J. Geophys. Res., 97, 11429–11441, https://doi.org/10.1029/92JC00876, 1992.

Andreas, E. L.: The Temperature of Evaporating Sea Spray Droplets., Journal of the Atmospheric Sciences, 52, 852–862, https://doi.org/10.1175/1520-0469(1995)052%3C0852:TTOESS%3E2.0.CO;2, 1995.

Andreas, E. L.: Approximation formulas for the microphysical properties of saline droplets, Atmospheric Research, 75, 323–345, https://doi.org/10.1016/j.atmosres.2005.02.001, 2005.

Andreas, E. L., Persson, P. O. G., and Hare, J. E.: A Bulk Turbulent Air–Sea Flux Algorithm for High-Wind, Spray Conditions, Journal of Physical Oceanography, 38, 1581–1596, https://doi.org/10.1175/2007JPO3813.1, 2008.

Andreas, E. L., Mahrt, L., and Vickers, D.: An improved bulk air–sea surface flux algorithm, including spray-mediated transfer, Quart J Royal Meteoro Soc, 141, 642–654, https://doi.org/10.1002/qj.2424, 2015.

Anguelova, M. D. and Webster, F.: Whitecap coverage from satellite measurements: A first step toward modeling the variability of oceanic whitecaps, J. Geophys. Res., 111, 2005JC003158, https://doi.org/10.1029/2005JC003158, 2006.

Babanin, A.: Breaking and dissipation of ocean surface waves, Cambridge University Press, 2011.

Bao, J.-W., Fairall, C. W., Michelson, S. A., and Bianco, L.: Parameterizations of sea-spray impact on the air–sea momentum and heat fluxes, Monthly Weather Review, 139, 3781–3797, 2011.

Barr, B. W., Chen, S. S., and Fairall, C. W.: Sea-State-Dependent Sea Spray and Air–Sea Heat Fluxes in Tropical Cyclones: A New Parameterization for Fully Coupled Atmosphere–Wave–Ocean Models, Journal of the Atmospheric Sciences, 80, 933–960, https://doi.org/10.1175/JAS-D-22-0126.1, 2023.

Bharti, V., Fairall, C. W., Blomquist, B. W., Huang, Y., Protat, A., Sullivan, P. P., Siems, S. T., and Manton, M. J.: Air-Sea Heat and Momentum Fluxes in the Southern Ocean, JGR Atmospheres, 124, 12426–12443, https://doi.org/10.1029/2018JD029761, 2019.

Bortkovskii, R. S.: Air-sea exchange of heat and moisture during storms, Springer Science & Business Media, 2013.

Bourassa, M. A., Gille, S. T., Bitz, C., Carlson, D., Cerovecki, I., Clayson, C. A., Cronin, M. F., Drennan, W. M., Fairall, C. W., and Hoffman, R. N.: High-latitude ocean and sea ice surface fluxes: Challenges for climate research, Bulletin of the American Meteorological Society, 94, 403–423, 2013.

Brumer, S. E., Zappa, C. J., Brooks, I. M., Tamura, H., Brown, S. M., Blomquist, B. W., Fairall, C. W., and Cifuentes-Lorenzen, A.: Whitecap Coverage Dependence on Wind and Wave Statistics as Observed during SO GasEx and HiWinGS, Journal of Physical Oceanography, 47, 2211–2235, https://doi.org/10.1175/JPO-D-17-0005.1, 2017.

Buck, A. L.: New Equations for Computing Vapor Pressure and Enhancement Factor, Journal of Applied Meteorology and Climatology, 20, 1527–1532, https://doi.org/10.1175/1520-0450(1981)020%3C1527:NEFCVP%3E2.0.CO;2, 1981.

Comiso, J.: Bootstrap Sea Ice Concentrations from Nimbus-7 SMMR and DMSP SSM/I-SSMIS, Version 4, NASA National Snow and Ice Data Center Distributed Active Archive Center (DAAC) data set, X5LG68MH013O, https://doi.org/10.5067/X5LG68MH013O, 2023.

Deike, L.: Mass Transfer at the Ocean–Atmosphere Interface: The Role of Wave Breaking, Droplets, and Bubbles, Annu. Rev. Fluid Mech., 54, 191–224, https://doi.org/10.1146/annurev-fluid-030121-014132, 2022.

Droghei, R., Nardelli, B. B., and Santoleri, R.: Combining In Situ and Satellite Observations to Retrieve Salinity and Density at the Ocean Surface, Journal of Atmospheric and Oceanic Technology, 33, 1211–1223, https://doi.org/10.1175/JTECH-D-15-0194.1, 2016.

Eichler, T. P. and Gottschalck, J.: A Comparison of Southern Hemisphere Cyclone Track Climatology and Interannual Variability in Coarse-Gridded Reanalysis Datasets, Advances in Meteorology, 2013, 891260, https://doi.org/10.1155/2013/891260, 2013.

Fairall, C., Kepert, J., and Holland, G.: The effect of sea spray on surface energy transports over the ocean, The Global Atmosphere and Ocean System, 2, 121–142, 1995.

Fairall, C. W., Edson, J. B., and Miller, M. A.: Heat Fluxes, Whitecaps, and Sea Spray, in: Surface Waves and Fluxes, edited by: Geernaert, G. L. and Plant, W. L., Springer Netherlands, Dordrecht, 173–208, https://doi.org/10.1007/978-94-009-2069-9_6, 1990.

Gall, J. S., Frank, W. M., and Kwon, Y.: Effects of sea spray on tropical cyclones simulated under idealized conditions, Monthly weather review, 136, 1686–1705, 2008.

Hersbach, H.: ERA5 monthly averaged data on single levels from 1940 to present, (No Title), 2023.

Hewson, T.: A Record Breaking Extratropical Cyclone in 2022: A Sign of Climate Change ?, Copernicus Meetings, https://doi.org/10.5194/ems2023-303, 2023.

Hosking, J. S., Orr, A., Marshall, G. J., Turner, J., and Phillips, T.: The Influence of the Amundsen–Bellingshausen Seas Low on the Climate of West Antarctica and Its Representation in Coupled Climate Model Simulations, Journal of Climate, 26, 6633–6648, https://doi.org/10.1175/JCLI-D-12-00813.1, 2013.

Hoskins, B. J. and Hodges, K. I.: A New Perspective on Southern Hemisphere Storm Tracks, Journal of Climate, 18, 4108–4129, https://doi.org/10.1175/JCLI3570.1, 2005.

Josey, S., Taylor, P. K., and Kent, E. C.: NOC 1.1: National Oceanography Centre Surface Flux Climatology (version 1.1), 2014.

Kepert, J., Fairall, C., and Bao, J.-W.: Modelling the Interaction Between the Atmospheric Boundary Layer and Evaporating Sea Spray Droplets, in: Air-Sea Exchange: Physics, Chemistry and Dynamics, vol. 20, edited by: Geernaert, G. L., Springer Netherlands, Dordrecht, 363–409, https://doi.org/10.1007/978-94-015-9291-8_14, 1999.

Kepert, J. D.: Comments on "The Temperature of Evaporating Sea Spray Droplets," 1996.

Liu, J., Xiao, T., and Chen, L.: Intercomparisons of air–sea heat fluxes over the Southern Ocean, Journal of Climate, 24, 1198–1211, 2011.

Liu, W. T., Katsaros, K. B., and Businger, J. A.: Bulk parameterization of air-sea exchanges of heat and water vapor including the molecular constraints at the interface, Journal of Atmospheric sciences, 36, 1722–1735, 1979.

Makin, V. K.: Air-sea exchange of heat in the presence of wind waves and spray, J. Geophys. Res., 103, 1137–1152, https://doi.org/10.1029/97JC02908, 1998.

Meredith, M. P., Sommerkorn, M., Cassotta, S., Derksen, C., Ekaykin, A. A., Hollowed, A. B., Kofinas, G., Mackintosh, A. N., Muelbert, M. M. C., Melbourne-Thomas, J., Ottersen, G., Pritchard, H. D., and Schuur, E. A. G.: Chapter 3: Polar Regions, in: The Ocean and Cryosphere in a Changing Climate: Summary for Policymakers, Intergovernmental Panel on Climate Change, 3–3, 2019.

Monahan, E. C., Spiel, D. E., and Davidson, K. L.: A Model of Marine Aerosol Generation Via Whitecaps and Wave Disruption, in: Oceanic Whitecaps, vol. 2, edited by: Monahan, E. C. and Niocaill, G. M., Springer Netherlands, Dordrecht, 167–174, https://doi.org/10.1007/978-94-009-4668-2_16, 1986.

Moura, R., Casagrande, F., and de Souza, R. B.: An Overview of Air-Sea Heat Flux Products and CMIP6 HighResMIP Models in the Southern Ocean, Atmosphere, 16, 402, https://doi.org/10.3390/atmos16040402, 2025.

Mueller, J. A. and Veron, F.: Impact of sea spray on air–sea fluxes. Part I: Results from stochastic simulations of sea spray drops over the ocean, Journal of Physical Oceanography, 44, 2817–2834, 2014a.

Mueller, J. A. and Veron, F.: Impact of Sea Spray on Air–Sea Fluxes. Part II: Feedback Effects, Journal of Physical Oceanography, 44, 2835–2853, https://doi.org/10.1175/JPO-D-13-0246.1, 2014b.

Myrhaug, D., Wang, H., and Holmedal, L. E.: Addendum to “Sea spray aerosol flux estimation based on long-term variation of wave statistics”: estimation based on long-term variation of wind statistics, Oceanologia, 58, 150–153, https://doi.org/10.1016/j.oceano.2015.11.003, 2016.

Ogle, S. E., Tamsitt, V., Josey, S. A., Gille, S. T., Cerovečki, I., Talley, L. D., and Weller, R. A.: Episodic Southern Ocean Heat Loss and Its Mixed Layer Impacts Revealed by the Farthest South Multiyear Surface Flux Mooring, Geophysical Research Letters, 45, 5002–5010, https://doi.org/10.1029/2017GL076909, 2018.

Perrie, W., Zhang, W., Andreas, E. L., Li, W., Gyakum, J., and McTaggart-Cowan, R.: Sea Spray Impacts on Intensifying Midlatitude Cyclones, Journal of the Atmospheric Sciences, 62, 1867–1883, https://doi.org/10.1175/JAS3436.1, 2005.

Petersen, G. N. and Renfrew, I. A.: Aircraft-based observations of air–sea fluxes over Denmark Strait and the Irminger Sea during high wind speed conditions, Quart J Royal Meteoro Soc, 135, 2030–2045, https://doi.org/10.1002/qj.355, 2009.

Priestley, M. D. K., Ackerley, D., Catto, J. L., Hodges, K. I., McDonald, R. E., and Lee, R. W.: An Overview of the Extratropical Storm Tracks in CMIP6 Historical Simulations, Journal of Climate, 33, 6315–6343, https://doi.org/10.1175/JCLI-D-19-0928.1, 2020.

Raphael, M. N., Marshall, G. J., Turner, J., Fogt, R. L., Schneider, D., Dixon, D. A., Hosking, J. S., Jones, J. M., and Hobbs, W. R.: The Amundsen Sea Low: Variability, Change, and Impact on Antarctic Climate, Bulletin of the American Meteorological Society, 97, 111–121, https://doi.org/10.1175/BAMS-D-14-00018.1, 2016.

Renfrew, I. A., Petersen, G. N., Sproson, D. a. J., Moore, G. W. K., Adiwidjaja, H., Zhang, S., and North, R.: A comparison of aircraft-based surface-layer observations over Denmark Strait and the Irminger Sea with meteorological analyses and QuikSCAT winds, Quarterly Journal of the Royal Meteorological Society, 135, 2046–2066, https://doi.org/10.1002/qj.444, 2009a.

Renfrew, I. A., Outten, S. D., and Moore, G. W. K.: An easterly tip jet off Cape Farewell, Greenland. I: Aircraft observations, Quarterly Journal of the Royal Meteorological Society, 135, 1919–1933, https://doi.org/10.1002/qj.513, 2009b.

Richter, D. H. and Sullivan, P. P.: The sea spray contribution to sensible heat flux, Journal of the Atmospheric Sciences, 71, 640–654, 2014.

https://doi.org/10.5194/essd-2026-476
Preprint. Discussion started: 31 August 2026

Schulz, E. W., Josey, S. A., and Verein, R.: First air-sea flux mooring measurements in the Southern Ocean, Geophysical Research Letters, 39, 2012GL052290, https://doi.org/10.1029/2012GL052290, 2012.

Smith, S. D.: Coefficients for sea surface wind stress, heat flux, and wind profiles as a function of wind speed and temperature, Journal of Geophysical Research: Oceans, 93, 15467–15472, https://doi.org/10.1029/JC093iC12p15467, 1988.

Song, Y., Qiao, F., Liu, J., Shu, Q., Bao, Y., Wei, M., and Song, Z.: Effects of Sea Spray on Large-Scale Climatic Features over the Southern Ocean, Journal of Climate, 35, 4645–4663, https://doi.org/10.1175/JCLI-D-21-0608.1, 2022.

Swart, S., Gille, S. T., Delille, B., Josey, S., Mazloff, M., Newman, L., Thompson, A. F., Thomson, J., Ward, B., and Du Plessis, M. D.: Constraining Southern Ocean air-sea-ice fluxes through enhanced observations, Frontiers in Marine Science, 6, 421, 2019.

Tomita, H., Hihara, T., Kako, S., Kubota, M., and Kutsuwada, K.: An introduction to J-OFURO3, a third-generation Japanese ocean flux data set using remote-sensing observations, J Oceanogr, 75, 171–194, https://doi.org/10.1007/s10872-018-0493-x, 2019.

Troitskaya, Y., Kandaurov, A., Ermakova, O., Kozlov, D., Sergeev, D., and Zilitinkevich, S.: Bag-breakup fragmentation as the dominant mechanism of sea-spray production in high winds, Scientific reports, 7, 1614, 2017.

Veron, F.: Ocean Spray, Annu. Rev. Fluid Mech., 47, 507–538, https://doi.org/10.1146/annurev-fluid-010814-014651, 2015.

Wang, Y., Kepert, J. D., and Holland, G. J.: The effect of sea spray evaporation on tropical cyclone boundary layer structure and intensity, Monthly weather review, 129, 2481–2500, 2001.

Woolf, D. K., Monahan, E. C., and Spiel, D. E.: Quantification of the marine aerosol produced by whitecaps, in: Preprints, 7th Conference on Ocean-Atmosphere Interaction, 182–185, 1988.

Xu, X., Voermans, J. J., Moon, I., Liu, Q., Guan, C., and Babanin, A. V.: Sea Spray Impacts on Tropical Cyclone Olwyn Using a Coupled Atmosphere-Ocean-Wave Model, JGR Oceans, 127, e2022JC018557, https://doi.org/10.1029/2022JC018557, 2022.

Yi, A., Liu, J., Renfrew, I. A., Yang, C., Dong, C., Song, X., and Yang, Q.: A Spray-Mediated Surface Turbulent Heat Flux Dataset for the Southern Ocean, Earth System Science Data, 2026.

Young, I. R. and Ribal, A.: Multiplatform evaluation of global trends in wind speed and wave height, Science, 364, 548–552, https://doi.org/10.1126/science.aav9527, 2019.

Young, I. R., Zieger, S., and Babanin, A. V.: Global Trends in Wind Speed and Wave Height, Science, 332, 451–455, https://doi.org/10.1126/science.1197219, 2011.

Yuan, X.: High-wind-speed evaluation in the Southern Ocean, J. Geophys. Res., 109, 2003JD004179, https://doi.org/10.1029/2003JD004179, 2004.

Zhao, D., Toba, Y., Sugioka, K., and Komori, S.: New sea spray generation function for spume droplets, J. Geophys. Res., 111, 2005JC002960, https://doi.org/10.1029/2005JC002960, 2006.

Zhao, Z., Shi, J., Wang, H., Yi, Z., Zhang, W., and Zhang, X.: Parameterization scheme of the sea surface drag coefficient considering the influence of wave states and sea spray stress, Front. Mar. Sci., 11, https://doi.org/10.3389/fmars.2024.1336709, 2024.